Coles, B. D, Hillier, A. D., Coomer, F. C., Bristowe, Nicholas C., Ramos, Silvia and McCabe, E. E. (2019) *Spin interactions and magnetic order in the iron oxychalcogenide BaFe2Q2O(Q=S and Se).* Physical Review B, 100 (2). ISSN 2469-9950.

Spin interactions and magnetic order in the iron oxychalcogenides BaFe$_2$Q$_2$O (Q = S and Se)

B. D. Coles,[1] A. D. Hillier,[2] F. C. Coomer,[2] N. C. Bristowe,[1] S. Ramos,[1,*] and E. E. McCabe[1,†]

[1]*School of Physical Sciences, University of Kent, Canterbury, Kent CT2 7NH, United Kingdom*
[2]*ISIS Facility, Rutherford Appleton Labs, Chilton Didcot OX11 0QX, United Kingdom*

The ability to tune the iron chalcogenides BaFe$_2$Q$_3$ from Mott insulators to metals and then superconductors with applied pressure has renewed interest in low-dimensional iron chalcogenides and oxychalcogenides. We report here a combined experimental and theoretical study on the iron oxychalcogenides BaFe$_2$Q$_2$O (Q = S, Se) and show that their magnetic behavior results from nearest-neighbor magnetic exchange interactions via oxide and selenide anions of similar strength, with properties consistent with more localized electronic structures than those of BaFe$_2$Q$_3$ systems.

I. INTRODUCTION

The study of iron oxychalcogenide materials has developed in parallel to the effort to understand iron-based superconductivity [1]. The strength of the correlations between electrons and the proximity of these materials to a Mott insulator transition are fundamental questions about the iron pnictide and iron chalcogenide superconductors [2,3] that need to be understood in these materials but also in related systems that do not display superconductivity. In this context, iron oxychalcogenides such as X_2O$_2$Fe$_2$OQ_2 (with X = La, Nd and Q = S, Se) are an important family to investigate, first, because they are structurally related to the superconductors and, second, because substitution of the chalcogenide ion allows for some tuning of the electronic bandwidth (and hence their proximity to a metal-insulator transition) [4].

The work presented in this paper was prompted by the report of superconductivity in the two-leg ladder materials BaFe$_2$Q$_3$ (Q = S, Se) under pressure [5–7]. This discovery has highlighted the importance of understanding not only the role of electronic structure and degree of electronic correlation in iron-based superconductors but also that of the crystal structure and dimensionality [8–11].

The crystal structure of BaFe$_2$Q$_3$ materials is composed of double chains of edge-linked FeQ_4 tetrahedra (the two-leg ladders) with ladders well separated from one another (by ∼6 Å) by barium cations [12,13]. This results in much stronger intraladder interactions than the interactions between ladders [14,15], with experimental work suggesting short-range antiferromagnetic (AFM) correlations well above the Néel temperature T_N [12,16]. Given the ratio of intraladder:interladder exchange, theoretical work supports the description of these systems as "pseudo-one-dimensional ladders," highlighting the nearly one-dimensional nature of the exchange interactions [15]. At ambient pressure, they can be described as orbital-selective Mott insulators [5,14]. With

increased pressure, BaFe$_2$Q$_3$ undergoes first an insulator-metal phase transition and, at higher pressures, a transition to a superconducting state [5–7]. These remarkable materials have led to renewed interest in iron ladder compounds [10,17], specifically, how their magnetic and electronic structures compare with related systems in terms of dimensionality and electron correlation.

The Mott insulating oxychalcogenides BaFe$_2$Q$_2$O studied in this work share some common features with the two-leg-ladder AFe$_2$Q$_3$ systems. Both contain tetrahedrally coordinated Fe^{2+} cations, but in BaFe$_2$Q$_2$O, the FeQ_3O tetrahedra are corner linked via oxide anions (along [010]), forming the "rungs" of ladders, and corner linked via chalcogenide anions (along [100]), forming the lengths of the ladders. These ladders are linked across edges of the FeQ_3O tetrahedra to give buckled Fe-Q-O layers, separated by barium cations [Fig. 1(a)]. The magnetic exchange interactions in BaFe$_2$Q$_2$O materials have been suggested to be quite anisotropic, with AFM Fe-O-Fe J_1 exchange along the ladder rungs thought to dominate [18–20]. This has given rise to their description as "spin ladders" [19,21–23], prompting our investigation using neutron powder diffraction (NPD) and muon spin relaxation methods to investigate their magnetic behavior. In contrast to AFe$_2$Q$_3$ systems, the Fe^{2+} coordination environment in BaFe$_2$Q$_2$O materials (with coordination by both oxide and softer chalcogenide anions and in buckled layers) is thought to narrow the Fe $3d$ bands [18], and so comparison with AFe$_2$Q$_3$ systems gives some insight into the effect of band narrowing in these materials. Our experimental work is complemented by a theoretical study to investigate the magnetic exchange interactions as a function of on-site Coulomb potential U_{Fe}; this illustrates how the BaFe$_2$Q$_2$O materials differ from the spin ladder AFe$_2$Q$_3$ systems and reveals the source of magnetic frustration and spin dynamics suggested by other experimental studies.

II. METHODS

Polycrystalline samples of BaFe$_2$S$_2$O and BaFe$_2$Se$_2$O were prepared by the solid-state reaction of stoichiometric

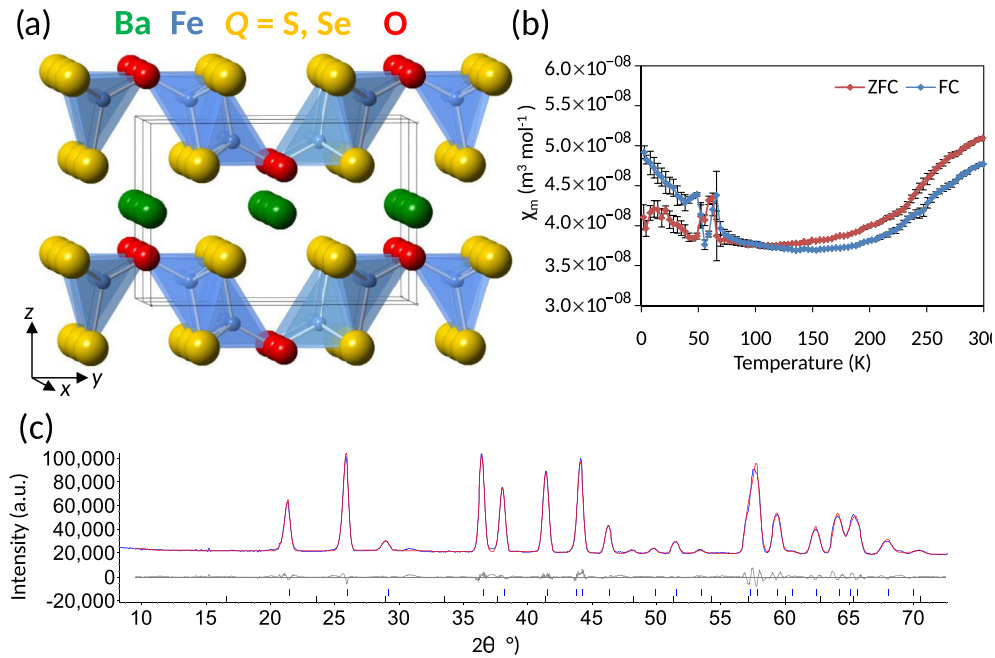*S.Ramos-Perez@kent.ac.uk
†e.e.mccabe@kent.ac.uk

FIG. 1. (a) Nuclear cell of BaFe$_2Q_2$O showing Ba, Fe, Q, and O ions in green, blue, yellow, and red, respectively. (b) Magnetic susceptibility data for BaFe$_2$S$_2$O and (c) Rietveld refinement profiles for BaFe$_2$S$_2$O using 293 K NPD data. Observed, calculated, and difference profiles are shown in blue, red, and gray, respectively; upper blue ticks and lower black ticks show reflection positions for BaFe$_2$S$_2$O and for Fe$_3$O$_4$ [1.13(2)% by weight], respectively.

quantities of BaO (99.99%), Fe powder (99%+), and S powder (99.5%) or Se powder (99.5%+). The reagents were weighed and ground by hand in an agate pestle and mortar in an Ar-filled glove box (H$_2$O < 0.5 ppm, $O_2 < 0.5$ ppm) and placed in small alumina crucibles. These were placed inside quartz reaction tubes which were evacuated and sealed under vacuum. The reaction tubes were heated slowly to a reaction temperature of 800 °C for BaFe$_2$S$_2$O and to 740 °C for BaFe$_2$Se$_2$O, held at this temperature for 24 h, and allowed to cool in the furnace. The reaction mixtures were then reground, pelletized, and sealed again in evacuated quartz tubes and heated slowly to the reaction temperature for a further 24 h before cooling in the furnace. Initial characterization was carried out using a Rigaku Miniflex600 x-ray powder diffractometer with copper source and nickel filter. Field-cooled (FC) and zero-field-cooled (ZFC) magnetic susceptibility data were collected on warming (at a rate of 5 °C min^{-1}) for ∼0.1 g of BaFe$_2$S$_2$O and on ∼0.04 g of BaFe$_2$Se$_2$O in fields from 1000 to 60 000 Oe (see Sec. III A). NPD data were collected for BaFe$_2$S$_2$O on the high-flux diffractometer D20 at the Institut Laue-Langevin (Grenoble, France) with a neutron wavelength of 2.41 Å. The powder was placed in a 10 mm diameter cylindrical vanadium can (to a height of 2.5 cm), and data were collected from 5° to 130° 2θ. Four 10-min scans were collected at 1.8 K, and 10-min scans were collected on warming at 2 K min^{-1} to 290 K. NPD data were collected for BaFe$_2$Se$_2$O on the time-of-flight diffractometer Wish on target station 2 at the ISIS spallation neutron and muon source (Rutherford Appleton Laboratory, United Kingdom). The powder was placed in a 6 mm diameter cylindrical vanadium can (to a height of 1 cm). A 60-min (40 μA) scan was collected at 2 K before the sample was heated to 245 K, with 60-min scans collected at 80 and 180 K and

20-min (13 μA) scans collected at intermediate temperatures at 5 K intervals. Rietveld refinements [24] were performed using TOPASACADEMIC software [25,26]. For refinements using constant-wavelength NPD data, the diffractometer zero point and neutron wavelength were refined using data collected at 160 K for which lattice parameters were known from X-ray powder diffraction (XRPD) analysis and were then fixed for subsequent refinements. A background was refined for each refinement, as well as unit cell (u.c.) parameters, atomic positions, and a pseudo-Voigt peak shape. Constant-wavelength NPD data were of lower resolution, and only data up to 70° 2θ were used in refinements; therefore, a single global isotropic temperature factor was used for all sites.

Temperature-dependent muon spin relaxation data in zero applied field were collected at EMU (ISIS spallation neutron and muon source, Rutherford Appleton Laboratory, United Kingdom). A closed-cycle refrigerator was used to vary the temperature between 400 and 10 K. The sample was 0.683 g of material in powder form, contained within Ag foil pouches (1.5 cm^2).

First-principles calculations based on density functional theory (DFT) were employed to determine the spin exchange interactions. All simulations made use of the VASP package [27,28], version 5.4.1. We chose the PBEsol [29] $+ U$ exchange correlation potential within the Liechtenstein [30] framework, where the effective on-site Coulomb and exchange parameters, U and J, were varied on the Fe d electrons within a sensible range of values [18]. To converge the total energy, force, and stress to within 0.5 meV/u.c., 0.5 meV/Å, and 0.02 GPa, respectively, we found that an 800 eV plane wave cutoff and $6 \times 2 \times 4$ k-point mesh for the 12-atom unit cell were necessary. Tests were made to check that the energy difference between single 12-atom and doubled

24-atom supercells were kept below 0.5 meV/u.c. using these parameters. Projector augmented-wave pseudopotentials [31] were used in the calculations with the following valence electron configuration: $5s^2\,5p^6\,6s^2$ (Ba), $3p^6\,4s^2\,3d^6$ (Fe), $4s^2\,4p^4$ (Se), $3s^2\,3p^4$ (S), and $2s^2\,2p^4$ (O). Atomic coordinates and lattice vectors were frozen to the low-temperature neutron data for the $BaFe_2S_2O$ and $BaFe_2Se_2O$ systems.

III. RESULTS

A. Magnetic susceptibility

Initial measurements for $BaFe_2Se_2O$ in 1000 Oe applied field (see the Supplemental Material [32]) suggested three phase transitions, consistent with single-crystal measurements reported by Lei *et al.* [20]. However, magnetization measurements as a function of field at 300 K indicated the presence of a FM component that saturates in a field of 10 000 Oe, and analogous results were found for $BaFe_2S_2O$ [32]. Field-cooled and zero-field-cooled susceptibility data [Fig. 1(b)] were obtained by subtracting data collected in an applied field of 45 000 Oe from those collected at 55 000 Oe (above the saturation level of the FM impurity). This method was used to subtract the contribution from ferromagnetic impurities (that order within this temperature range) and reveal the behavior of the bulk sample. These results indicate that Curie-Weiss behavior is not observed over the whole temperature range for either sample, and the changes in slope at 240 K for $BaFe_2Se_2O$ and at 250 K for $BaFe_2S_2O$ indicate the development of long-range magnetic order below these temperatures, consistent with other reports [19–21]. In these corrected data, the anomaly in susceptibility at ∼115 K, also observed by Lei *et al.* [20], is absent, suggesting that this may arise from a FM impurity phase such as Fe_3O_4 [33]. However, the low-temperature feature (at $T_2 \sim 59$ K for $BaFe_2S_2O$ and at $T_2 \sim 40$ K for $BaFe_2Se_2O$) is still observed and may indicate freezing of some spin dynamics, as discussed further below.

B. Room-temperature NPD data

NPD data collected above T_N for both $BaFe_2Se_2O$ and $BaFe_2S_2O$ are consistent with the reported crystal structures [18,21]. Preliminary refinements were carried out to investigate sample stoichiometry, with the Ba site occupancy fixed at unity and a single overall temperature factor. These refinements indicated that both samples were close to their ideal stoichiometries, although slightly iron and chalcogenide deficient ($BaFe_{1.966(3)}Se_{1.982(3)}O_{0.991(3)}$ and $BaFe_{1.935(5)}S_{1.87(1)}O_{0.985(8)}$); sites were assumed to be fully occupied in subsequent analysis of the long-range magnetic structures. Refinements to investigate possible anion-disorder indicated full ordering of oxide and chalcogenide anions for both samples. Final refinement details and profiles are given in Table I and Fig. 1(c). Both samples were found to contain traces of impurities, including Fe_3O_4, consistent with magnetic susceptibility data discussed above [$BaFe_2Se_2O$ contained 3.66(3)% Fe_3O_4 by weight and 2.02(1)% FeSe by weight; $BaFe_2S_2O$ contained 1.13(1)% Fe_3O_4 by weight]. There was no evidence in these room-temperature NPD data of any diffuse scatter that might result from short-range magnetic correlations or short-range order.

TABLE I. Refinement details and selected distances, bond lengths, and angles from Rietveld refinements using 293 K NPD data for $BaFe_2S_2O$ and 275 K NPD data for $BaFe_2Se_2O$ using the *Pmmn* nuclear model for both.

X	$Q = $ S, 300 K	$Q = $ Se, 275 K
a (Å)	4.0038(2)	4.13425(9)
b (Å)	9.5729(6)	9.8516(1)
c (Å)	6.4765(4)	6.7202(1)
Volume (Å^3)	248.23(2)	273.705(7)
Ba $2a$ z	0.5276(6)	0.5103(2)
Ba $U_{iso} \times 100$ (Å^2)	1.4(2)	1.07(5)
Fe $4e$ y	0.6684(2)	0.6642(6)
Fe $4e$ z	0.8797(3)	0.87971(9)
Fe $U_{iso} \times 100$ 100 (Å^2)	1.4(2)	1.74(3)
Se $4e$ y	0.7880(8)	0.79261(7)
Se $4e$ z	0.766(1)	0.7588(1)
Se $U_{iso} \times 100$ 100 (Å^2)	1.4(2)	1.39(3)
O $2b$ z	0.7310(7)	0.7394(1)
O $U_{iso} \times 100$ 100 (Å^2)	1.4(2)	1.49(5)
R_{wp} (%)	3.40	3.68
R_p (%)	2.51	4.13
χ^2	33.32	13.75
Fe-Fe [010] (Å)	3.225(5)	3.235(1)
Fe-Fe [111] (Å)	2.979(3)	3.1217(8)
Fe-O (Å)	1.878(3)	1.8723(8)
Fe-Q [001] (Å)	2.331(7)	2.4660(9)
Fe-Q [110] (Å)	2.420(5)	2.5560(5)
Fe-O-Fe (deg)	118.3(3)	119.54(7)
Fe-Q-Fe [100] (deg)	111.6(3)	107.95(3)
Fe-Q-Fe [111] (deg)	77.63(1)	76.84(2)

C. Low-temperature NPD analysis and magnetic structure

No additional reflections were observed in low-temperature NPD data, but the intensity of $0kl$ and $hk0$ reflections increased smoothly on cooling, while there was little change in $0k0$ reflections (see the Supplemental Material [32]). These observations were consistent with long-range, three-dimensional magnetic order developing below T_N with k vector $k = (000)$. ISODISTORT [34] was used to obtain descriptions of possible magnetic structures consistent with this k vector. The collinear $\Gamma1-$ AFM structure (Fig. 2), with moments oriented along [010] with AFM coupling across Fe-O-Fe rungs (J_1) and between ladders (J_3) but FM coupling along ladder legs (J_2), gave a good fit to the data, and this model was used for subsequent analysis. This magnetic structure can be described by $Pm'm'n'$ symmetry, and we note that this $\Gamma1-$ model also allows an AFM out-of-plane component. This cants the moments slightly away from the [010] direction to lie closer to the Fe-O bond direction, and including this additional parameter gave a very slight improvement in fit (R_{wp} decreased from 3.807% to 3.785% for $BaFe_2S_2O$ and from 3.392% to 3.376% for $BaFe_2Se_2O$). This allows a small AFM component of the moment along [001] and, at 2 K, results in Fe^{2+} moments canted at ∼5°. Given the slight improvement in fit and the small refined component along [001], we cannot confirm this canting from our NPD data (a good fit is obtained with moments
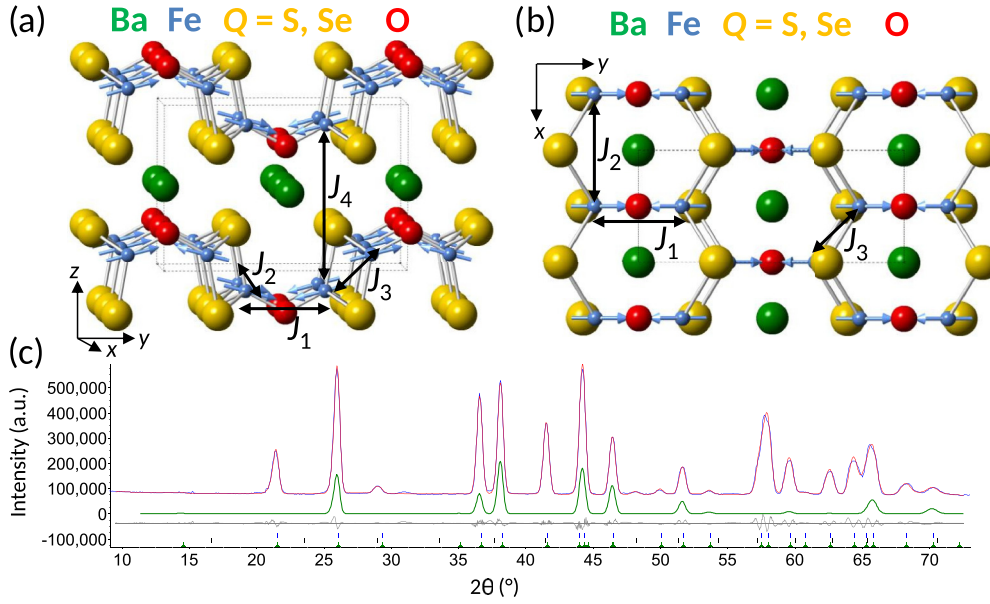
FIG. 2. Illustration of $\Gamma1-$ magnetic structure showing Fe^{2+} moments as blue arrows, viewed down (a) the [100] direction and (b) the [001] direction, and (c) refinement profiles for $BaFe_2S_2O$ using 2 K NPD data with observed, calculated, and difference profiles shown in blue, red, and gray, respectively; upper blue ticks, middle black ticks, and lower green ticks show reflection positions for $BaFe_2S_2O$, Fe_3O_4, and the magnetic phase, respectively, and scattering from the magnetic phase is highlighted in green.

oriented along [010]), and no change in moment direction could be detected on cooling (see the Supplemental Material [32]). However, this symmetry-allowed [001] component is compatible with fluctuations of the moments within the (011) planes that might eventually freeze out at low temperature, as discussed further below. Details from low-temperature refinements are given in Table II. The magnetic structure is illustrated in Fig. 2 with refinement profiles (see also the Supplemental Material [32]).

D. Variable-temperature NPD analysis

Sequential refinements were carried out using variable-temperature NPD data and indicated that the unit cell parameters for both phases decrease smoothly on cooling (Fig. 3 and Supplemental Material [32]). No additional reflections were observed, and there was no evidence to suggest changes to the long-range crystal structure or symmetry on cooling. Possible structural distortions were considered but did not give improvements in fit. We cannot rule out the possibility that a short-range Peierls-like distortion as observed for $BaFe_2Se_3$ [12] may occur as our analysis of the long-range, average structure will not be sensitive to this. For $BaFe_2S_2O$, the Fe-O and second-nearest-neighbor Fe-Fe distance (along [010]) decrease more abruptly below T_N, also decreasing the Fe-O-Fe angle. The Fe-S-Fe angles change very little on cooling, while the Fe-S [001] bond length (bridging between the ladders) increases below T_N, as does the interladder Fe-Fe distance (labeled Fe-Fe [111]; Fig. 3). This is in contrast to the selenide analog, $BaFe_2Se_2O$, for which all bond lengths and Fe-Fe distances decrease smoothly on cooling [32]. The evolution of the magnetic order in $BaFe_2Q_2O$ can be fitted to critical behavior (Fig. 4), with critical exponents of 0.319(6) for $BaFe_2S_2O$ and 0.190(5) for $BaFe_2Se_2O$.

TABLE II. Refinement details and selected distances, bond lengths, and angles from Rietveld refinements using 1.8 K NPD data for $BaFe_2S_2O$ and 2 K NPD data for $BaFe_2Se_2O$ using the *Pmmn* nuclear model and the $\Gamma1-$ magnetic model for both.

| X	$Q =$ S, 1.8 K	$Q =$ Se, 2 K
a (Å)	3.9975(1)	4.12633(6)
b (Å)	9.5460(5)	9.8378(1)
c (Å)	6.4528(2)	6.7006(1)
Volume (Å^3)	246.24(2)	272.004(8)
Ba $2a$ z	0.5319(8)	0.5111(2)
Ba U_{iso} × 100 (Å^2)	1.0(3)	0.25(5)
Fe $4e$ y	0.6657(3)	0.66391(6)
Fe $4e$ z	0.8823(3)	0.88159(8)
Fe U_{iso} × 100 (Å^2)	1.0(3)	0.80(3)
Fe moment (units of μ_B)	3.17(3)	3.39(1)
Fe moment along [010] (units of μ_B)	3.16(3)	3.38(1)
Fe moment along [001] (units of μ_B)	0.25(6)	0.33(2)
Se $4e$ y	0.7831(9)	0.79209(6)
Se $4e$ z	0.757(1)	0.75776(9)
Se U_{iso} × 100 (Å^2)	1.0(3)	0.63(4)
O $2b$ z	0.7316(8)	0.7380(1)
O U_{iso} × 100 (Å^2)	1.0(3)	0.59(5)
R_{wp} (%)	3.78	3.38
R_p (%)	2.84	3.99
χ^2	33.32	12.12
Fe-Fe [010] (Å)	3.163(5)	3.225(1)
Fe-Fe [111] (Å)	2.982(3)	3.1053(7)
Fe-O (Å)	1.857(3)	1.8779(8)
Fe-Q [001] (Å)	2.379(7)	2.4550(8)
Fe-Q [110] (Å)	2.430(5)	2.5564(4)
Fe-O-Fe (deg)	116.8(3)	118.35(7)
Fe-Q-Fe [100] (deg)	111.6(3)	107.62(2)
Fe-Q-Fe [111] (deg)	76.6(2)	76.55(2)
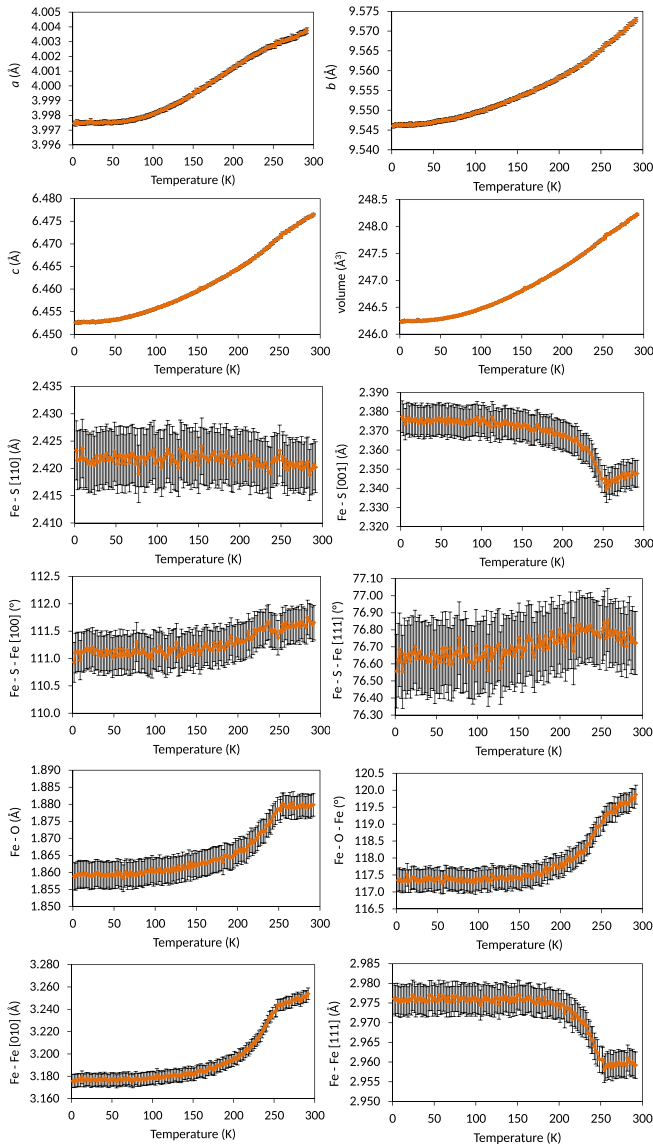
FIG. 3. Unit cell parameters and selected distances, bond angles, and lengths for $BaFe_2S_2O$ from sequential refinements using variable-temperature NPD data.
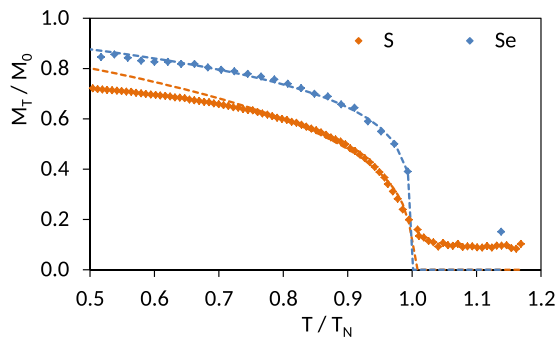

FIG. 4. Evolution of magnetic order for $BaFe_2Q_2O$. Data points are solid symbols, and the dashed lines are guides to the eye showing critical behavior $M_T = M_0[1 - (\frac{T}{T_N})]^\beta$, where critical exponent $\beta = 0.319(6)$, $T_N = 249.7(1)$ K, and $M_0 = 4.22(4)\mu_B$ for $BaFe_2S_2O$ and critical exponent $\beta = 0.190(5)$, $T_N = 241.6(2)$ K, and $M_0 = 3.95(3)\mu_B$ for $BaFe_2Se_2O$.
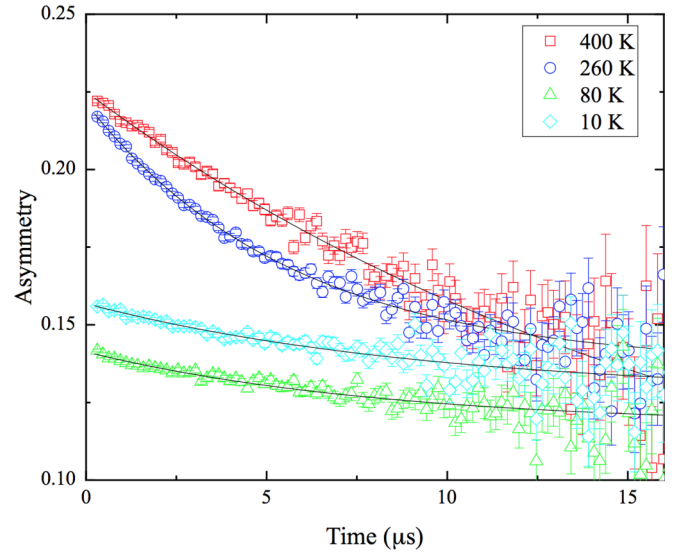

FIG. 5. ZF asymmetry data for $BaFe_2Se_2O$ at 400, 260, 80, and 10 K. The four data sets illustrate the different magnetic environments encountered by the muons as a function of temperature as well as the quality of the fits to the model presented in Eq. (1).

E. Muon spin relaxation analysis for $BaFe_2Se_2O$

Muon spin relaxation (μSR) asymmetry data collected in zero applied field (ZF) were carried out at several temperatures to characterize the behavior of the material across the transitions identified through the magnetization measurements. Magnetization and NPD have shown similar magnetic behavior between the two systems, and hence, we anticipate the additional understanding provided by μSR measurements is likely to apply to both. The evolution with time of the asymmetry for $BaFe_2Se_2O$ was fitted using a simple exponential decay plus a constant background:

$$A(t) = A_0 e^{-\lambda t} + A_{\text{back}}, \qquad (1)$$

where A_{back} is the flat background, A_0 is the initial asymmetry, λ is the relaxation constant, and t is time. The background constant was fitted for the temperature region where the depolarization rate is the fastest (around 150 K), where it took a value of 0.11 ± 0.01. This was then fixed as the value of A_{back} for the fits at every other temperature. The higher than usual value is due to the fact that the sample was loaded in several individual pouches of silver foil.

The four sets of raw data shown in Fig. 5 are representative of the different types of magnetic behavior observed in this material as a function of temperature. Figure 6 shows the values of the two fitting parameters at all measured temperatures and allows us to identify two transitions. The first one, at ∼240 K, is consistent with the AFM ordering transition at T_N, observed also in the magnetization measurements and by temperature-dependent neutron diffraction. The signature of the transition in the relaxation constant is noticeably broader than might have been expected for a typical three-dimensional magnetic phase transition, and this may reflect the quasi-two-dimensional nature of the magnetic correlations above T_N observed in magnetic susceptibility data and emphasized by Han *et al.* [18]. In addition, the ZF muon relaxation data show
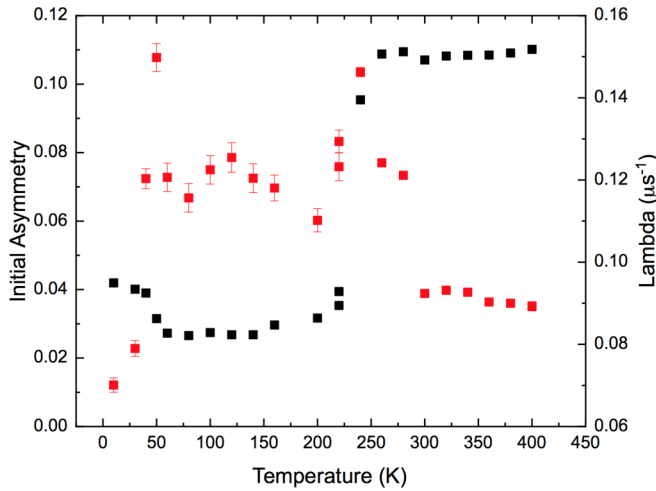
FIG. 6. Evolution of the initial asymmetry (in black) and relaxation rate λ (in red) as a function of temperature. Both fitting parameters show the presence of two transitions (at $\sim$240 and $\sim$40 K). Note that the transition at $\sim$240 K has a broader signature in temperature than that at $\sim$50 K.

the presence of a second transition at a lower temperature, around 40–50 K, consistent with the low-temperature transition T_2 observed in magnetic susceptibility measurements (see the Supplemental Material [32] and Fig. 1). As discussed above, NPD data are not sensitive to this magnetic transition, suggesting that it may correspond to a dynamic process. The μSR measurements are sensitive to spin fluctuations with timescales typically in the range between 10^{-12} and 10^{-5} s and can detect slower dynamics than neutron scattering. A possible interpretation of this result is that the magnetically ordered state at 240 K contains moments whose canting is fluctuating at a rate for which neutron diffraction would only be sensitive to the average structure. This low-temperature transition below 40 K may involve freezing out of the spin fluctuations within the (011) planes (which are allowed by the model used to fit the diffraction data) to give ordered components along both [010] and [001] below $\sim$50 K, resulting in an increase of the initial asymmetry as seen by the muons.

F. Electronic structure calculations

We performed electronic structure calculations to estimate the exchange interactions for the material. Figure 2 illustrates the four spin interactions we investigate in BaFe$_2$Q$_2$O: J_1 Fe-O-Fe ($\sim$120°) across the rungs of the ladder, J_2 Fe-Q-Fe ($\sim$110°) along the legs of the ladder, J_3 interladder Fe-Q-Fe ($\sim$77°) interactions, and interlayer J_4 interactions. To determine the theoretical values of these exchange interactions, six ordered spin states [one FM (Γ4+) and five AFM states], presented in Fig. 7, were considered. Γ1$-$ (the model suggested by analysis of NPD data) and Γ2+ both contain AFM J_1 (across the ladder rungs) and FM J_2 (along the ladder lengths) but differ in the sign of the interladder J_3 exchange, with AFM J_3 for Γ1$-$ and FM J_3 for Γ2+. The Γ3$-$ model is similar to the Γ1$-$ model with FM J_2 (along the ladder lengths) and AFM interladder J_3 but differs with respect to FM J_1 (across the ladder rungs). The X2 model is analogous to the
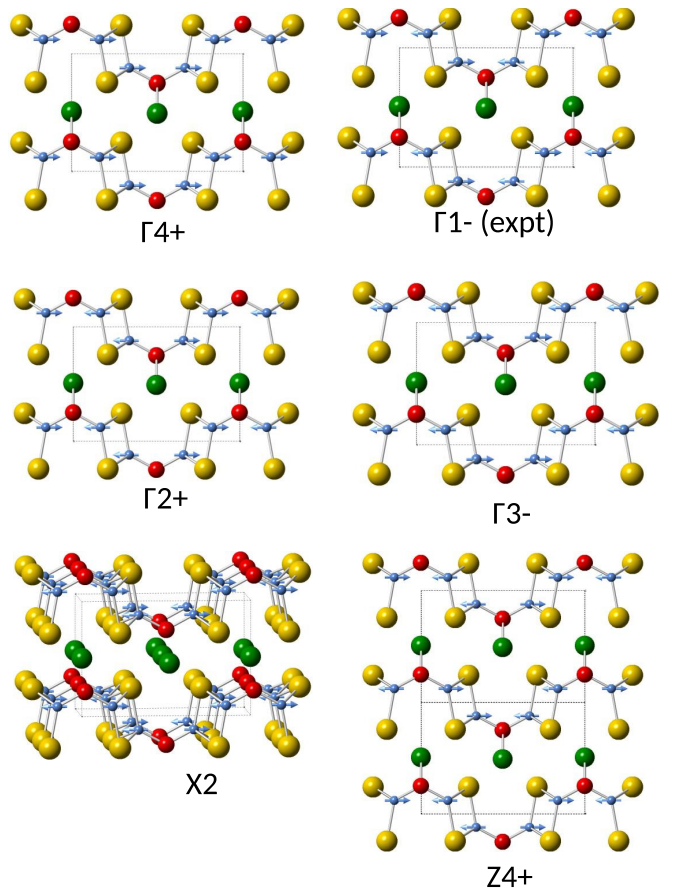

FIG. 7. Five ordered spin states, FM (Γ4+) and AFM Γ1$-$ (observed experimentally), Γ2+, Γ3$-$, X2, and Z4+, used to determine exchange interactions J_1–J_4 for BaFe$_2$Q$_2$O, with barium, iron, chalcogenide, and oxide ions shown in green, blue, yellow, and red, respectively, and Fe^{2+} spins shown by blue arrows.

Γ1$-$ model but with AFM J_2 (along the ladder lengths), requiring doubling of the magnetic unit cell along [100]. These five models allow the three intralayer exchange interactions to be determined, but the weaker interlayer J_4 interactions require a magnetic unit cell doubled along [001], and so the Z4+ model with AFM J_4 was also considered.

The experimentally observed magnetic structure, Γ1$-$, is the calculated ground state for the range of on-site Coulomb repulsion U_{Fe} studied (see Table III). The Γ1$-$ and Γ2+ models differ only in the sign of the interladder J_3 interaction, and the large difference in energies of these two models clearly indicates strong and AFM J_3 interactions. Likewise, the Γ1$-$ and Γ3$-$ models differ in the sign of J_1 exchange, and again, the relative energies of these models indicate that J_1 interactions are also strong and AFM. The AFM model X2, with AFM J_1 and AFM J_2 (in which half the J_3 interactions are FM and half are AFM), is stabilized with respect to the FM model (and also the Γ2+ and Γ3$-$ models with FM J_3 and J_1, respectively) but not to the extent of the Γ1$-$ model with FM J_2, suggesting that the J_2 exchange along the ladders is much weaker than the J_1 and J_3 exchange interactions. It is interesting that the FM model is found to be metallic for lower values of U_{Fe} ($U_{Fe} = 2.0$, 3.5, and 5.0 eV for $Q =$ S

TABLE III. Energies (in meV per unit cell) of AF spin arrangements shown in Fig. 7 relative to the $\Gamma1-$ AFM arrangement for various U_{Fe} values (in eV) for $BaFe_2Q_2O$. Where data are missing, either calculations were not performed, or the magnetic ordering produced a metallic ground state.

U_{Fe}	Q	$\Gamma2+$	$\Gamma4+$	$\Gamma3-$	X2[a]	Z4+[a]
2.0	S			401		
3.5	S	778		309	114	776
5.0	S	689	939	234	102	687
6.5	S	597	783	175	86	596
2.0	Se			369	95	659
3.5	Se			279	101	671
5.0	Se	583	792	208	87	580
6.5	Se	495	649	153	71	493

[a]Values for these doubled magnetic cells were halved for comparison with the other $k = (000)$ magnetic models.

and $U_{Fe} = 2.0$, 3.5 for $Q = $ Se), consistent with theoretical calculations reported by Han *et al.* [18].

The total spin exchange energies of these magnetic models can be expressed in terms of the spin Hamiltonian,

$$H = -\sum_{i,j} J_{i,j} \vec{S}_i \cdot \vec{S}_j, \tag{2}$$

where $J_{i,j}$ is the spin exchange interaction between spin sites i and j and can take values J_1 to J_4, as appropriate. By applying the energy expression for spin dimers with N unpaired spins per spin site (four for Fe^{2+}), the total spin energies per unit cell can be written as

$$E = (n_1 J_1 + n_2 J_2 + n_3 J_3 + n_4 J_4)\left(\frac{N_{Fe}^2}{4}\right), \tag{3}$$

where $N_{Fe} = 4$ and the coefficients n_1 to n_4 for the five spin ordered states are given in the Supplemental Material [32].

The relative energies of these magnetic models can be used, with energies for the models calculated from Eq. (3), to determine theoretical values of the exchange interactions, as shown in Table IV [35–40]. In contrast to the theoretical work by Han *et al.* [18], this analysis suggests that the relative strength of the Fe-O-Fe J_1 interaction, compared with the Fe-Q-Fe J_2 interaction, increases with U.

Our calculations suggest that longer-range exchange interactions (beyond next-nearest neighbor) are negligible, as

TABLE IV. Values of J_1, J_2, J_3, and J_4 (in meV) from energy-mapping analyses based on various U_{Fe} values (in eV) for $BaFe_2Q_2O$.

U_{Fe}	Q	J_1	J_2	J_3	J_4
2.0	S	−25.1			
3.5	S	−19.3	−8.6	−24.3	−0.1
5.0	S	−14.6	−7.6	−21.5	−0.1
6.5	S	−10.9	−6.6	−18.7	−0.1
2.0	Se	−23.1			
3.5	Se	−17.5			
5.0	Se	−13.0	−6.4	−18.2	−0.1
6.5	Se	−9.6	−5.5	−15.5	−0.1

suggested previously by Han *et al.* [18]; this is supported by calculations for the doubled unit cells X2 and Z4+, whose total energies are consistent with only J_{1-4} interactions. Indeed, the very low values calculated for J_4 (see Table IV) equal zero within the uncertainty expected for these calculations ($\sim$0.1 meV).

A value of $U_{Fe} = 3.5$ eV appears to simultaneously minimize both the maximum force on any species and the stress on the lattice, suggesting $U_{Fe} = 3.5$ eV would likely produce a relaxed structure closest to experiment [32]. This value of U_{Fe} also produces a magnetic moment close to experiment [for $BaFe_2Se_2O$, $\mu_{Fe} = 3.45 \mu_B$ from calculations, compared with $3.39(1) \mu_B$ from experiment; see Table II] and hence might be a good estimate of the on-site Coulomb repulsion of Fe in this environment.

IV. DISCUSSION

Analysis of our powder diffraction and magnetic susceptibility results for $BaFe_2Q_2O$ are consistent with experimental results reported by Valldor *et al.* [21] and Huh *et al.* [22] which illustrate the difficulty in preparing samples free from Fe_3O_4 and FeQ impurities. The traces of Fe_3O_4 (demonstrated unambiguously for our samples by combined NPD and magnetic susceptibility data) make it likely that the magnetic phase transition at $\sim$115 K reported by Lei *et al.* [20] (and observed in our low-magnetic-field susceptibility data; see the Supplemental Material [32]) is likely the Verwey transition in Fe_3O_4 [33].

The NPD data presented here also give information on the long-range, average crystal structure, and within the sensitivity of the refinements, there is no evidence for antisite disorder (although we cannot rule out this possibility at a more local scale, as suggested by Lei *et al.* [20] from Mössbauer results). Similarly, Popovic *et al.* [19] suggested that a structural change may occur on cooling below T_N based on Raman spectroscopy data for $BaFe_2Se_2O$, and although our NPD data give no evidence for a change in symmetry, there is a clear change in the iron coordination environment at T_N with contraction of Fe-Fe distances (along the ladder rungs) as the Fe-O and Fe-O-Fe bond lengths and angles both decrease (see Fig. 3 and the Supplemental Material [32]). In terms of interladder distances (Fe-Q [001] and Fe-Fe [111]), while these contract slightly on cooling for $BaFe_2Se_2O$ (see the Supplemental Material [32]), surprisingly, both distances increase noticeably below T_N for $BaFe_2S_2O$.

These changes in Fe^{2+} coordination environment at T_N are likely coupled to the magnetic ordering, and the increasing interladder distance might be expected to weaken the interladder exchange J_3. We note that this AFM interaction competes with the much weaker AFM J_2 exchange along the lengths of the ladders but with a similar degree of frustration for both $BaFe_2Se_2O$ and $BaFe_2S_2O$ (see further discussion below), it is unclear why this structural change occurs (which is likely to weaken J_3) in the sulfide analog and not the selenide.

A short-range spin-Peierls-like distortion was observed from neutron pair-distribution function analysis for the two-leg ladder system $BaFe_2Se_3$ [12]. These two-leg ladder systems contain double chains of FeQ_4 tetrahedra and have more itinerant electronic structures [41]. It is unlikely that such

distortions would occur in the more localized $BaFe_2Q_2O$ materials ($U_{Fe} \sim 3.5$ eV). In addition, our time-of-flight NPD data for $BaFe_2Se_2O$ (see the Supplemental Material [32]) might have been expected to show diffuse scattering if local distortions had occurred. However, we cannot rule out the presence of local distortions, as our analysis of the long-range, average crystal structure has limited sensitivity to them.

The experimentally observed magnetic structure for $BaFe_2Q_2O$ (Fig. 2) is similar to that proposed by Han *et al.* and is consistent with magnetization measurements on single crystals, which suggested that the easy axis of magnetization is within the *ab* plane [18]. This structure is also in agreement with Mössbauer studies on $BaFe_2S_2O$ and on $SrFe_2Q_2O$ ($Q =$ S, Se) by Huh *et al.* [22] and Valldor *et al.* [21], which indicated a simple, collinear AFM structure for these systems, and similar to the magnetic structure reported by Guo *et al.* for $SrFe_2Q_2O$ [23]. The magnitudes of the magnetic moments determined from NPD refinements [3.15(3) μ_B and 3.31(1) μ_B for $BaFe_2S_2O$ and $BaFe_2Se_2O$, respectively; see Table II] are similar to those reported for other insulating iron oxychalcogenides (e.g., 3.14(8) μ_B for $Ce_2O_2FeSe_2$ [40] and 3.50(2) μ_B for $La_2O_2Fe_2OSe_2$ [42]) and in the parent phase to superconducting $K_{0.8}Fe_{1.6}Se_2$ (3.31 μ_B) [43].

This $\Gamma1-$ magnetic structure can be understood in terms of the dominant AFM exchange interactions J_3 and J_1. The comparable strengths of these exchange interactions (Table IV) bring into question earlier descriptions of these $BaFe_2Q_2O$ systems as spin ladders [19,21–23] because the interladder exchange J_3 is comparable to or stronger than J_1 (across the ladder rungs) depending on U_{Fe}. The weak FM coupling along the lengths of the ladders results from two strong AFM J_3 interactions between the Fe^{2+} sites in adjacent ladders, frustrating the weaker AFM J_2 exchange between Fe^{2+} sites along the length of the ladder. We note that the energy of a single J_2 interaction is comparable to the energy of the low-temperature feature in magnetic susceptibility data and observed in muon spin relaxation experiments ($T_2 \sim 59$ K for $BaFe_2S_2O$; $T_2 \sim 40$ K for $BaFe_2Se_2O$). This frustration between J_2 and J_3 along the lengths of the ladder may result in some local/dynamic disorder for $T_2 \sim < T < T_N$ that freezes out at low temperatures below T_2 when J_2 becomes comparable to k_BT. NPD data showed no evidence for any diffuse magnetic scatter that might arise from such disorder but may not be sensitive to this if the fluctuations are very small or are slower than the neutron timescale ($\sim 10^{-13}$ s). It is likely that such spin fluctuations exist below T_N (with moments, on average, along [010]) before freezing out (to give the small AFM-ordered [001] component; Fig. 2) T_2, as observed in μSR data.

The presence of frustration has been considered by Huh *et al.* [22] and by Valldor *et al.* [21] in the strontium analogs. It is interesting that the results of our DFT calculations suggest a very similar degree of frustration (in terms of the relative magnitudes of J_2 and J_3; Table IV) for these two barium analogs. Huh *et al.* [22] and Valldor *et al.* [21] note the higher degree of frustration for the strontium analogs $SrFe_2Q_2O$ and suggest that this might relate to the size of the Fe-*Q*-Fe angles; our DFT results indicate that the degree of frustration relates to the relative magnitude of J_2 and J_3, which will be very sensitive to

the Fe-*Q*-Fe angles, consistent with their hypothesis. Further calculations for the strontium analogs would be of interest to confirm this.

The analysis of the dimensionality of the magnetic order does not give a conclusive answer. Our DFT calculations show that the in-plane exchange interactions J_1, J_2, and J_3 are noticeably stronger than the interlayer coupling J_4 (Table IV), and so it is unsurprising that magnetic susceptibility (see Fig. 1 and the Supplemental Material [32]) and heat capacity measurements [18] suggest short-range, two-dimensional magnetic correlations above T_N. However, given the relatively high temperatures for T_N below which magnetic Bragg scattering is observed and that there is a clear drop in the asymmetry of the muon decay (suggesting three-dimensional magnetic order), it is surprising that such low values are calculated for J_4. We note that these observations are similar to those for $BaFe_2Q_3$, with evidence for short-range magnetic correlations above T_2 [12,16,44] and interladder interactions of the same order of magnitude as J_4 interactions calculated here [14,15]. This may indicate deficiencies in our model; for example, the magnetic anisotropy of the Fe^{2+} site has been shown to be significant in other iron oxychalcogenides [42] but has been neglected in this current study. Further calculations including the effects of spin-orbit coupling would be of interest to investigate this further. It is worth noting that the critical exponents β (see Fig. 4) are similar to those expected for three- and two-dimensional Ising systems for $BaFe_2S_2O$ and $BaFe_2Se_2O$, respectively. Given the similar values for exchange interactions calculated by DFT for these two materials, it is not clear why there should be a significant difference in their magnetic dimensionalities. This question remains open, and it is, in our opinion, worthy of further study both by experiments and computationally.

Recently, we became aware of the magnetic structure reported for $SrFe_2Q_2O$ [23], which is consistent with our findings here for $BaFe_2Q_2O$, suggesting that our conclusions are likely to apply to a wide range of materials in this structural family.

V. CONCLUSIONS

Our results suggest that the magnetic insulators $BaFe_2Q_2O$ differ from spin ladder systems such as the superconducting $BaFe_2Q_3$ materials because the nearest-neighbor exchange interactions via oxide and selenide anions are of comparable strength, giving rise to stronger magnetic coupling. The more localized electronic structure with narrower Fe $3d$ bands (due to the harder oxide in the Fe^{2+} coordination environment and the buckled Fe-*Q*-O layers [18]) results in large ordered moments on the Fe^{2+} site in both the sulfide and selenide analogs, similar to other insulating oxychalcogenides. Although it would be interesting to investigate the extent to which the electronic structure of $BaFe_2Q_2O$ materials could be tuned by electron doping and applied pressure, the narrow Fe $3d$ bands (suggested by Han *et al.* [18] and consistent with our theoretical and experimental work) are likely to place the $BaFe_2Q_2O$ materials farther into the Mott insulating side than other Fe^{2+} spin ladder systems.

[1] Y. Yamihara, T. Watanabe, M. Hirano, and H. Hoson, J. Am. Chem. Soc. **130**, 3296 (2008).

[2] Q. Si and E. Abrahams, Phys. Rev. Lett. **101**, 076401 (2008).

[3] M. R. Norman, Physics **1**, 21 (2008).

[4] J.-X. Zhu, R. Yu, H. Wang, L. L. Zhao, M. D. Jones, J. Dai, E. Abrahams, M. Morosan, M. Fang, and Q. Si, Phys. Rev. Lett. **104**, 216405 (2010).

[5] T. Yamauchi, Y. Hirata, Y. Ueda, and K. Ohgushi, Phys. Rev. Lett. **115**, 246402 (2015).

[6] H. Takahashi, A. Sugimoto, Y. Nambu, T. Yamauchi, Y. Hirata, T. Kawakami, M. Avdeev, K. Matsubayashi, F. Du, C. Kawashima, H. Soeda, S. Nakano, Y. Uwatoko, Y. Ueda, T. J. Sato, and K. Ohgushi, Nat. Mater. **14**, 1008 (2015).

[7] J. Ying, H. Lei, C. Petrovic, Y. Xiao, and V. V. Struzhkin, Phys. Rev. B **95**, 241109(R) (2017).

[8] A. Hisada, K. Matsubayashi, Y. Uwatoko, N. Fujiwara, G. Deng, E. Pomjakushina, K. Conder, D. M. Radheep, R. Thiyagarajan, S. Esakkimuthu, and S. Arumugam, J. Phys. Soc. Jpn. **83**, 073703 (2014).

[9] J. M. Pizarro and E. Bascones, Phys. Rev. Mater. **3**, 014801 (2019).

[10] Y. Zhang, L.-F. Lin, J.-J. Zhang, E. Dagotto, and S. Dong, Phys. Rev. B **97**, 045119 (2018).

[11] Y. Gu, Z. Liu, T. Xie, W. Zhang, D. Gong, D. Hu, X. Ma, C. Li, L. Zhao, L. Lin, Z. Xu, G. Tan, G. Chen, Z. Y. Meng, Y.-F. Yang, H. Luo, and S. Li, Phys. Rev. Lett. **119**, 157001 (2017).

[12] J. M. Caron, J. R. Neilson, D. C. Miller, A. Llobet, and T. M. McQueen, Phys. Rev. B **84**, 180409(R) (2011).

[13] H. Y. Hong and H. Steinfink, J. Solid State Chem. **5**, 93 (1972).

[14] M. Mourigal, S. Wu, M. B. Stone, J. R. Neilson, J. M. Caron, T. M. McQueen, and C. L. Broholm, Phys. Rev. Lett. **115**, 047401 (2015).

[15] B. Saparov, S. Calder, B. Sipos, H. Cao, S. Chi, D. J. Singh, A. D. Christianson, M. D. Lumsden, and A. S. Sefat, Phys. Rev. B **84**, 245132 (2011).

[16] H. Lei, H. Ryu, A. I. Frenkel, and C. Petrovic, Phys. Rev. B **84**, 214511 (2011).

[17] K. T. Lai, P. Adler, Y. Prots, Z. Hu, C.-Y. Kuo, T.-W. Pi, and M. Valldor, Inorg. Chem. **56**, 12606 (2017).

[18] F. Han, X. Wan, B. Shen, and H.-H. Wen, Phys. Rev. B **86**, 014411 (2012).

[19] Z. V. Popovic, M. Scepanovic, N. Lazarevic, M. M. Radonjic, D. Tanaskovic, H. Lei, and C. Petrovic, Phys. Rev. B **89**, 014301 (2014).

[20] H. Lei, H. Ryu, V. Ivanovski, J. B. Warren, A. I. Frenkel, B. Cekic, W.-G. Yin, and C. Petrovic, Phys. Rev. B **86**, 195133 (2012).

[21] M. Valldor, P. Adler, Y. Prots, U. Burkhardt, and L. H. Tjeng, Eur. J. Inorg. Chem. **2014**, 6150 (2014).

[22] S. Huh, Y. Prots, P. Adler, L. H. Tjeng, and M. Valldor, Eur. J. Inorg. Chem. **2015**, 2982 (2015).

[23] H. Guo, M.-T. Fernandez-Diaz, A. C. Komarek, S. Huh, P. Adler, and M. Valldor, Eur. J. Inorg. Chem. **2017**, 3829 (2017).

[24] H. M. Rietveld, J. Appl. Crystallogr. **2**, 65 (1969).

[25] A. A. Coelho, J. Appl. Crystallogr. **36**, 86 (2003).

[26] A. A. Coelho, *Topas Academic: General profile and structure analysis software for powder diffraction data*, Bruker AXS: Karlsruhe, Germany, 2012.

[27] G. Kresse and J. Hafner, Phys. Rev. B **47**, 558(R) (1993).

[28] G. Kresse and J. Furthmüller, Comput. Mater. Sci. **6**, 15 (1996).

[29] J. P. Perdew, A. Ruzsinszky, G. I. Csonka, O. A. Vydrov, G. E. Scuseria, L. A. Constantin, X. Zhou, and K. Burke, Phys. Rev. Lett. **100**, 136406 (2008).

[30] A. I. Liechtenstein, V. I. Anisimov, and J. Zaanen, Phys. Rev. B **52**, R5467(R) (1995).

[31] P. E. Blöchl, Phys. Rev. B **50**, 17953 (1994).

[32] See Supplemental Material at http://link.aps.org/supplemental/10.1103/PhysRevB.100.024427 for additional magnetization and diffraction data and details on the DFT calculation.

[33] E. J. W. Verwey, Nature (London) **144**, 327 (1939).

[34] B. J. Campbell, H. T. Stokes, D. E. Tanner, and D. M. Hatch, J. Appl. Crystallogr. **39**, 607 (2006).

[35] M.-H. Whangbo, H.-J. Koo, and D. Dai, J. Solid State Chem. **176**, 417 (2003).

[36] D. Dai, M.-H. Whangbo, H.-J. Koo, X. Rocquefelte, S. Jobic, and A. Villesuzanne, Inorg. Chem. **44**, 2407 (2005).

[37] H. J. Xiang, C. Lee, H.-J. Koo, X. G. Gong, and M.-H. Whangbo, Dalton Trans. **42**, 823 (2013).

[38] D. Dai and M.-H. Whangbo, J. Chem. Phys. **114**, 2887 (2001).

[39] D. Dai and M.-H. Whangbo, J. Chem. Phys. **118**, 29 (2003).

[40] E. E. McCabe, C. Stock, J. L. Bettis, Jr., M.-H. Whangbo, and J. S. O. Evans, Phys. Rev. B **90**, 235115 (2014).

[41] K. Takubo, Y. Yokoyama, H. Wadati, S. Iwasaki, T. Mizokawa, T. Boyko, R. Sutarto, F. He, K. Hashizume, S. Imaizumi, T. Aoyama, Y. Imai, and K. Ohgushi, Phys. Rev. B **96**, 115157 (2017).

[42] E. E. McCabe, C. Stock, E. E. Rodriguez, A. S. Wills, J. W. Taylor, and J. S. O. Evans, Phys. Rev. B **89**, 100402(R) (2014).

[43] W. Bao, Q.-Z. Huang, G.-F. Chen, M. A. Green, D.-M. Wang, J.-B. He, and Y.-M. Qiu, Chin. Phys. Lett. **28**, 086104 (2011).

[44] Z. Seidov, H.-A. Krug von Nidda, V. Tsurkan, I. G. Filippova, A. Günther, T. P. Gavrilova, F. G. Vagizov, A. G. Kiiamov, L. R. Tagirov, and A. Loidl, Phys. Rev. B **94**, 134414 (2016).